We are very grateful to the evaluations from the reviewers, which have allowed us to clarify and improve the manuscript. Below we addressed the reviewer comments, with the reviewer comments in black and our response in **blue**.

Reply for the referee comment#2

General Comments: This manuscript presents a comprehensive modeling study of HOMs (Highly Oxygenated Organic Molecules) derived from monoterpenes using the CAM6-Chem global climate model. The authors implement a semi-explicit HOM chemical mechanism, extend the volatility basis set (VBS), and conduct a suite of sensitivity experiments to explore the impacts of branching ratios, autoxidation rates, and NOx levels on HOMs-SOA formation. The study is timely and addresses a significant gap in the representation of HOMs in global models. The methodology is sound, and the model development is well-documented. However, a major weakness of the manuscript lies in the limited and underdeveloped discussion of the results, particularly those from the global model simulations. The current treatment of global HOMs-SOA distributions lacks the depth and detail expected for a study of this scope and importance. This significantly reduces the scientific value and interpretability of the findings. For this reason, I recommend major revisions, with particular emphasis on expanding and deepening the analysis of the global model results. Additionally, improvements are needed in the clarity of some sections, including the presentation of the chemical mechanism.

Response: Thank you very much for the reviewer's thoughtful review and valuable comments. In response to the suggestions, we have strengthened the analysis and discussion of the global simulation results, and improved the clarity of the chemical mechanism presentation. All relevant issues raised have been carefully addressed in the revised manuscript. Detailed responses to each comment are provided below.

Major comments

1. Expansion of the discussion on global model results

The current discussion of global HOMs-SOA distributions (Section 3.3) is relatively brief and lacks depth. I strongly recommend expanding this analysis and relocating it to a new Section 4 to allow for a more comprehensive and focused discussion, including:

- A more detailed regional analysis beyond SEUS, SECN, and Amazon. For example, Europe, South Asia, and Africa are not discussed despite being relevant for OMs and/or biogenic and anthropogenic interactions.
- A more thorough treatment of seasonality, including regional seasonal cycles and their drivers (e.g., oxidant levels, emissions).
- A spatially resolved analysis of how HOMs-SOA distributions change across the nine sensitivity experiments. This could include difference maps or regional statistics showing the impact of branching ratios and autoxidation rates.
- Consideration of vertical distributions of HOMs-SOA, especially given their relevance for new particle formation and cloud interactions.

Response: We sincerely thank the reviewer for the insightful and constructive comments. We have substantially expanded the analysis of global HOMs-SOA distributions and moved this discussion to a new Section 4, as suggested. The updated content of Section 4 is as follows:

4 Spatial and temporal distribution of HOMs-SOA

4.1 Spatial and distribution of HOMs-SOA

Globally, the annual mean concentration of HOMs-SOA is 0.0556 μg m^{-3}, accounting for 13.3 % of total SOA and 37.3 % of MTSOA (Fig. 12). Across the sensitivity experiments, the contribution of HOMs-SOA to total SOA varies between 6 % and 15 % (Fig. 9). The HighYield (15 %) and LowYield (6 %) experiments encompass the uncertainty range reported in Xu et al. (2022) and highlight the dominant influence of the MT-bRO_2 branching ratio on HOMs-SOA formation. The effect of autoxidation rates is secondary, as indicated by the Fast (14 %) and Slow (10 %) experiments (Fig. 12), where the differences are moderate and consistent with the rate-dependent parameterizations proposed by Weber et al. (2021). In contrast, the influence of NO levels is negligible, with the Low~~NOx~~NO (13 %) and no_HMB_NO (11 %) experiments indicating that anthropogenic NO emissions exert little impact on the global HOMs-SOA concentration. Similarly, the contribution of HOMs-SOA to MTSOA ranges from 19 % to 41 % across the sensitivity experiments, with the highest fraction in HighYield and the lowest in LowYield, further highlighting the critical role of the MT-bRO_2 branching ratio in determining the HOMs-SOA contribution.

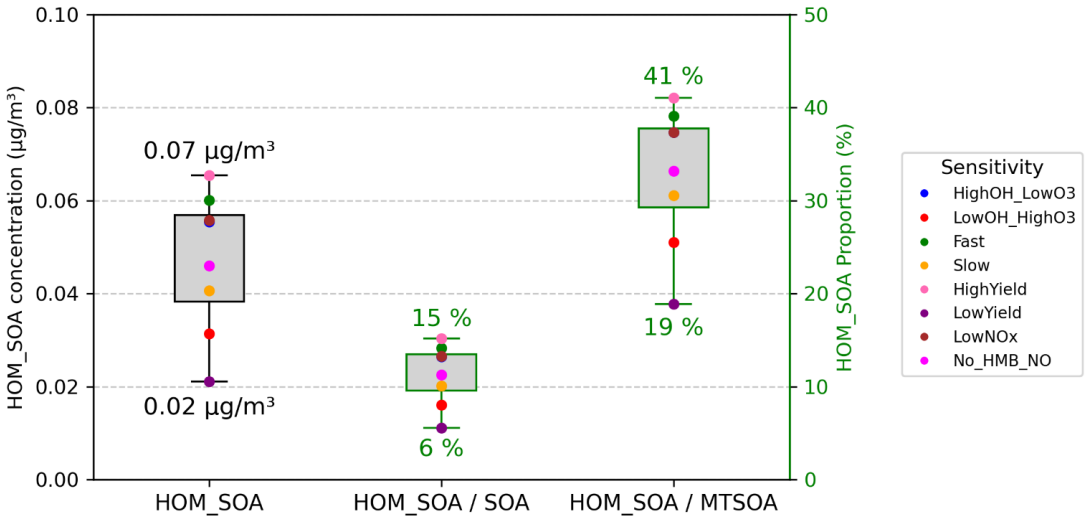

Figure 9. *The global averaged value of 2013 annual mean surface HOMs-SOA (unit: μg/m3), the contribution of HOMs-SOA to the total SOA and MTSOA (unit: %) using different sensitivity tests (Table 8). The specific value of different tests is shown in Table S14.*

The contribution of HOMs-SOA to total SOA and MTSOA shows pronounced spatial variability globally (Fig. 10). In the Control experiment, HOMs-SOA concentrations are highest in tropical and parts of mid-latitude regions, particularly over the Amazon rainforest, central Africa, the southeastern United States, and Australia, where warm and humid conditions coincide with high biogenic emissions (Fig. 10a). In these regions, HOMs-SOA typically accounts for more than 10 % of total SOA, with some areas exceeding 40 % (Fig. 10b), and contributes more than 20 % to MTSOA (Fig. 10c). Also, in regions strongly influenced by anthropogenic emissions, such as Southeast Asia and Europe, the contribution of HOMs-SOA to MTSOA remains substantial, consistent with the role of anthropogenic NO in HOM formation (Fig. 3).

Across the sensitivity experiments, the spatial patterns of HOMs-SOA contributions to total SOA and MTSOA are generally consistent with those in the Control experiment (Fig. S7). In the HighYield experiment, the contribution of HOMs-SOA to MTSOA exceeds 30 % over most tropical regions with high biogenic emissions. In contrast, in the LowYield experiment, the contribution to MTSOA drops markedly across most regions, falling below 15 %. These results indicate that uncertainties in the MT-bRO₂ branching ratio not only affect the global mean but also amplify the contrast between biogenically dominated regions and other areas. Changes in the Fast and Slow experiments are more moderate, occurring mainly over high-emission regions and their downwind areas, where Fast increases the HOMs-SOA contribution to MTSOA by ~5%, while Slow yields comparable decreases. By comparison, the NO-related experiments (LowNO and no_HMB_NO) show limited changes in most regions, with slight decreases (< 2%) in both MTSOA and total SOA contributions over high-NO emission regions such as East Asia and Europe. These results further support that, although NO can alter HOM composition under polluted conditions, its influence on the global burden and spatial distribution of HOMs-SOA is minimal.

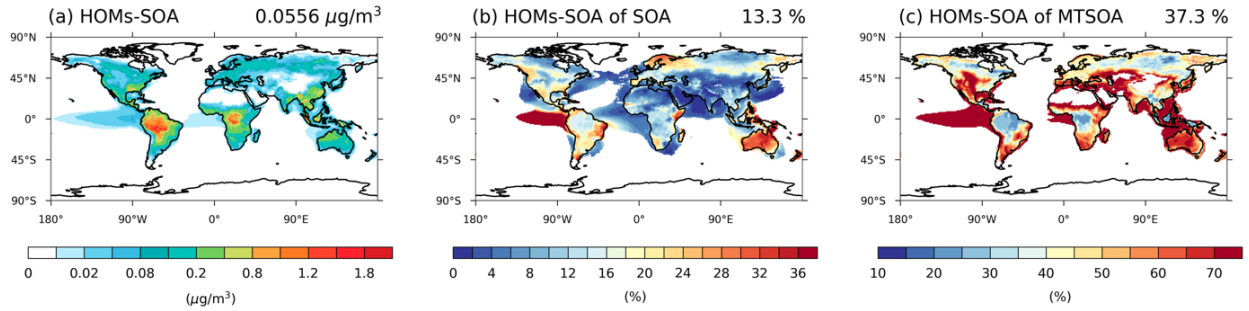

Figure 10. *2013 annual averaged surface (a) HOMs-SOA (unit: μg/m3), (b) the contribution of HOMs-SOA to the MTSOA and (c) the contribution of HOMs-SOA to the total SOA (unit: %) in Control experiment. The global averaged value is shown in upper right corner of each figure. Proportions are only shown in regions where MTSOA or total SOA is greater than 10% of the global average.*

Vertically, HOMs-SOA is primarily concentrated in the near-surface and lower troposphere (below 800 hPa), reflecting its close link to surface biogenic emissions (Fig. 11). There are significant regional differences in the contribution of HOMs-SOA to total SOA between the Northern and Southern Hemispheres. In most regions of the Northern Hemisphere, anthropogenic emissions dominate, leading to a low contribution from biogenic HOMs-SOA (<10%). In contrast, the contribution increases markedly in the Southern Hemisphere (>14%). This difference is largely driven by the high emissions of monoterpenes and isoprene in tropical regions, such as the Amazon and central Africa (Fig. S4), which promote the substantial formation of HOMs-SOA, especially C15 and C20 (Fig. 12). These compounds are then transported to higher altitudes through deep convection. As a result, HOMs-SOA remains at high concentrations in the 400–200 hPa range in the tropics, contributing more than 20% to SOA at these altitudes (Fig. 11). Additionally, gaseous HOMs may also be transported to higher layers, where they significantly enhance new particle formation, influencing cloud condensation nuclei (CCN) concentrations (Shao et al., 2024; Zhao et al., 2024), and further affecting cloud properties and radiative effects (Shao et al., 2025).

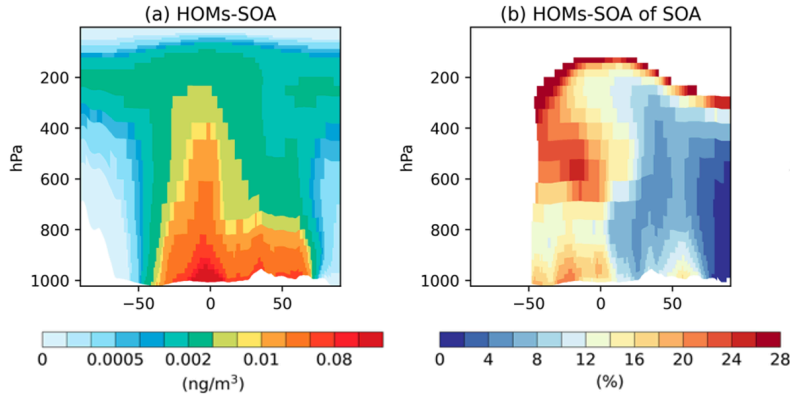

Figure 11. *Vertical distribution of 2013 annual averaged (a) HOMs-SOA concentration (μg/m³) and (b) proportion of HOMs-SOA to total SOA (%) in the Control experiment. The global average value is shown in the upper right corner of each panel. Proportions are only shown in regions where total SOA is greater than 10% of the global average.*

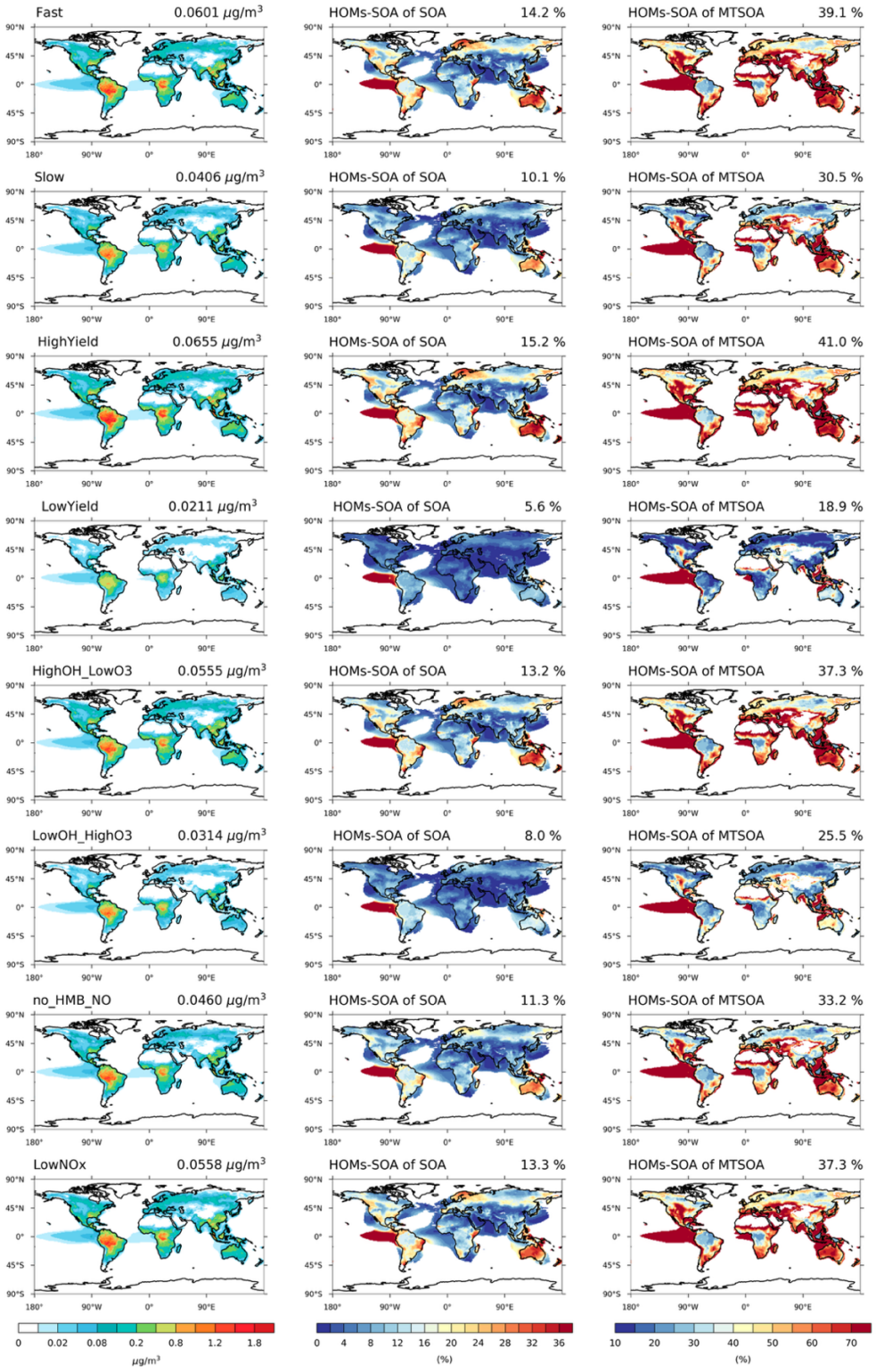

Figure S7. *Global distribution of HOMs-SOA concentrations (μg/m³) and their contributions to SOA (middle column) and MTSOA (right column) across different sensitivity experiments. The global average value is displayed in the upper right corner of each panel. Proportions are only shown in regions where MTSOA or total SOA is greater than 10% of the global average.*

4.2 Temporal variation of HOMs-SOA

On a global scale, the seasonal variation of HOMs-SOA are primarily determined by the intensity of biogenic emissions (monoterpenes and isoprene), with a more significant effect in the Northern Hemisphere summer (Fig. 13). The levels of oxidants (OH and O_3), however, play a greater role in modulating the relative contribution of different HOM species (Figs. 12 and 14). In high NO regions, such as the United States (US), Southeast Asian continental regions (SECN), and Europe (EUR), the concentrations of OH and O_3 facilitate the formation of MT-HOM-RO_2. Combined with higher NO concentrations, this promotes the generation of C_{10}-ON (Fig. 3). In contrast, in low NO tropical regions, such as the Amazon and central Africa (CAF), the proportion of low-volatility dimers (C_{15} and C_{20}) significantly increases.

In tropical regions, the absolute concentration of HOMs-SOA is significantly higher than in mid-latitudes, with a greater proportion of dimers (C_{15} and C_{20}) (Fig. 12). The annual mean concentration in the AMZ is 0.90 μg/m³, peaking during the dry season (August–October) at approximately 1.4 μg/m³. During this period, monoterpene (~230 ng/m³) and isoprene (~900 ng/m³) emissions are elevated (Fig. 13), while reduced wet deposition favors the formation of C_{15} and C_{20} dimers. As a result, the dimer fraction reaches 58%, with C_{15} contributing 34% and C_{20} contributing 24%. O_3 concentrations (Fig. 14) also promote multi-step autoxidation reactions. Meanwhile, the relatively low anthropogenic emissions in the Amazon result in low NO concentrations, preventing the rapid formation of C_{10}-ON via NO reactions with MT-HOM-RO_2 (Fig. 3). Instead, MT-HOM-RO_2 undergoes self- and cross-reactions to form dimers. Similarly, the CAF region exhibits similar characteristics, with an annual mean concentration of 0.47 μg/m³, maintaining relatively high levels throughout the year. During the peak emission period (January–May), both C_{15} and C_{20} levels increase simultaneously (Fig. 12). These findings highlight that low NO emissions and high biogenic emissions play an important role in the generation dimers.

Mid-latitude regions exhibit significant seasonal variations, with a higher proportion of C_{10}-ON (Fig. 12). In regions such as the US, SECN, and EUR, a clear summer peak occurs between June and August, corresponding to significant increases in monoterpene and isoprene emissions (Fig. 13). South Asia (SAS) shows a bimodal distribution, with higher emissions in March–May and October–November, respectively. During the rainy season (June–September), enhanced wet deposition leads to reduced biogenic emissions, resulting in a bimodal distribution of HOMs-SOA (Fig. 13). In the Southern Hemisphere, Australia (AUS) exhibits a seasonal peak opposite to that of the Northern Hemisphere (occurring from October to March) (Fig. 13), but the seasonal distribution still remains consistent with biogenic emissions (Fig. 13). In these regions, where anthropogenic NO emissions are high, the proportion of C_{10}-ON (exceeding 60%) is significantly higher than that of dimers, highlighting the dominant role of the MT-HOM-RO_2 + NO termination reaction under high NO conditions.

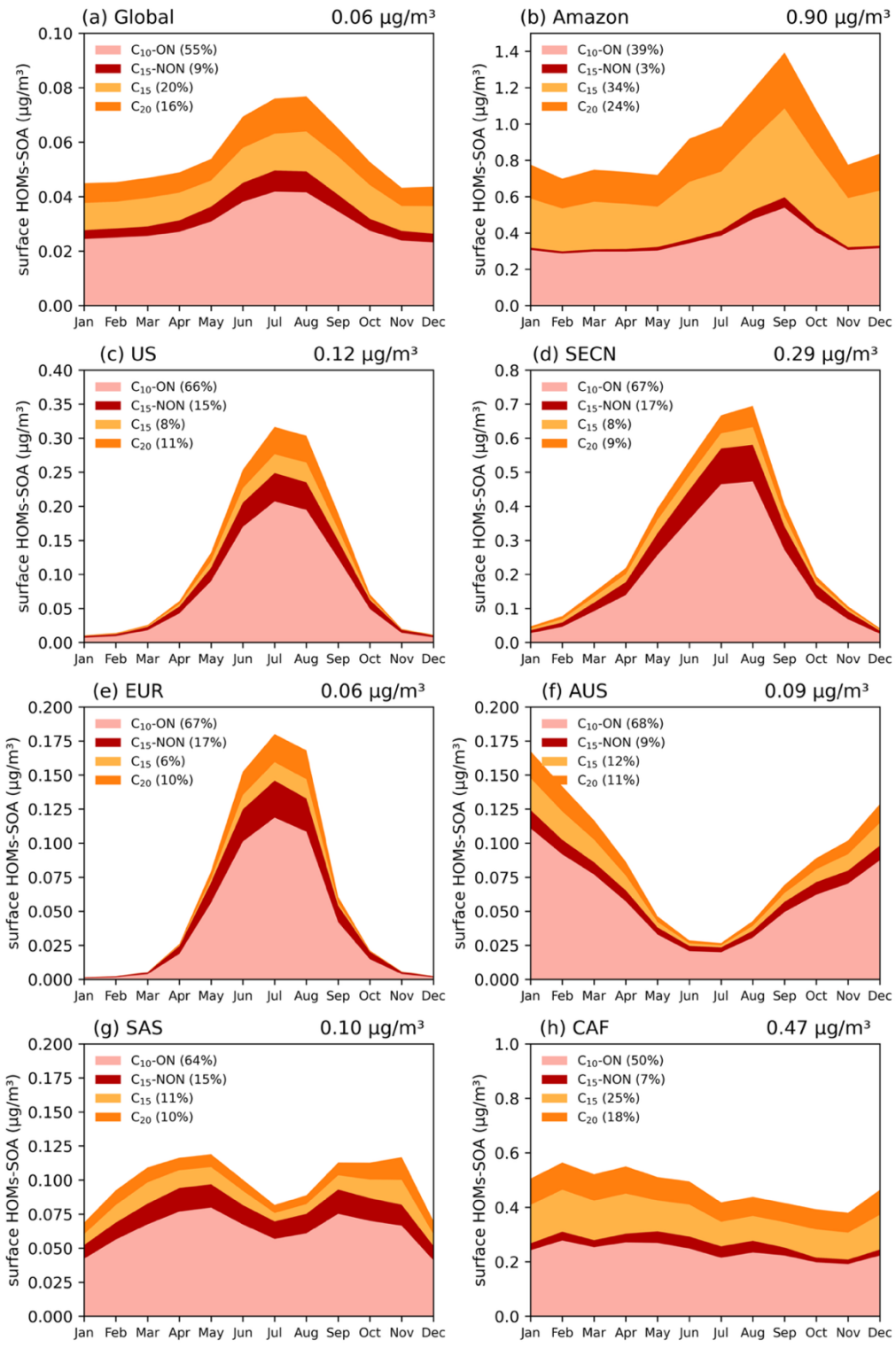

Figure 12. *Seasonal variations of HOMs-SOA concentrations (μg/m³) in different regions. The contributions of C_{10}-ON, C_{10}-NON, C_{15}, and C_{20} are shown in different colors, with the percentage contribution of each component indicated in the legend. Details of each geographic region can be found in Figure S9.*

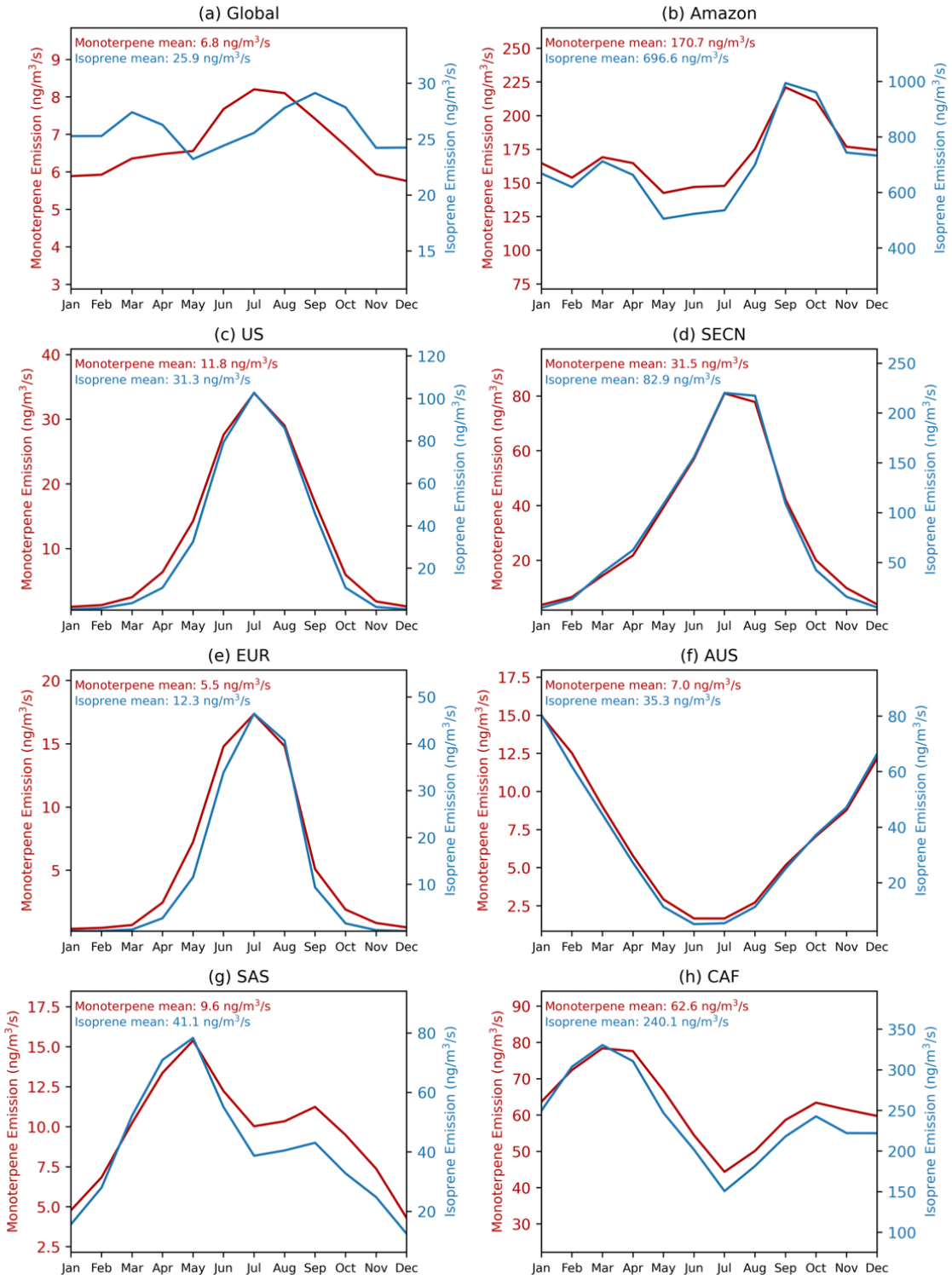

Figure 13. *Seasonal variations in monoterpene and isoprene emissions (ng/m³/s) across different regions. The average annual emissions for each species are provided in the caption. Details of each geographic region can be found in Figure S9.*

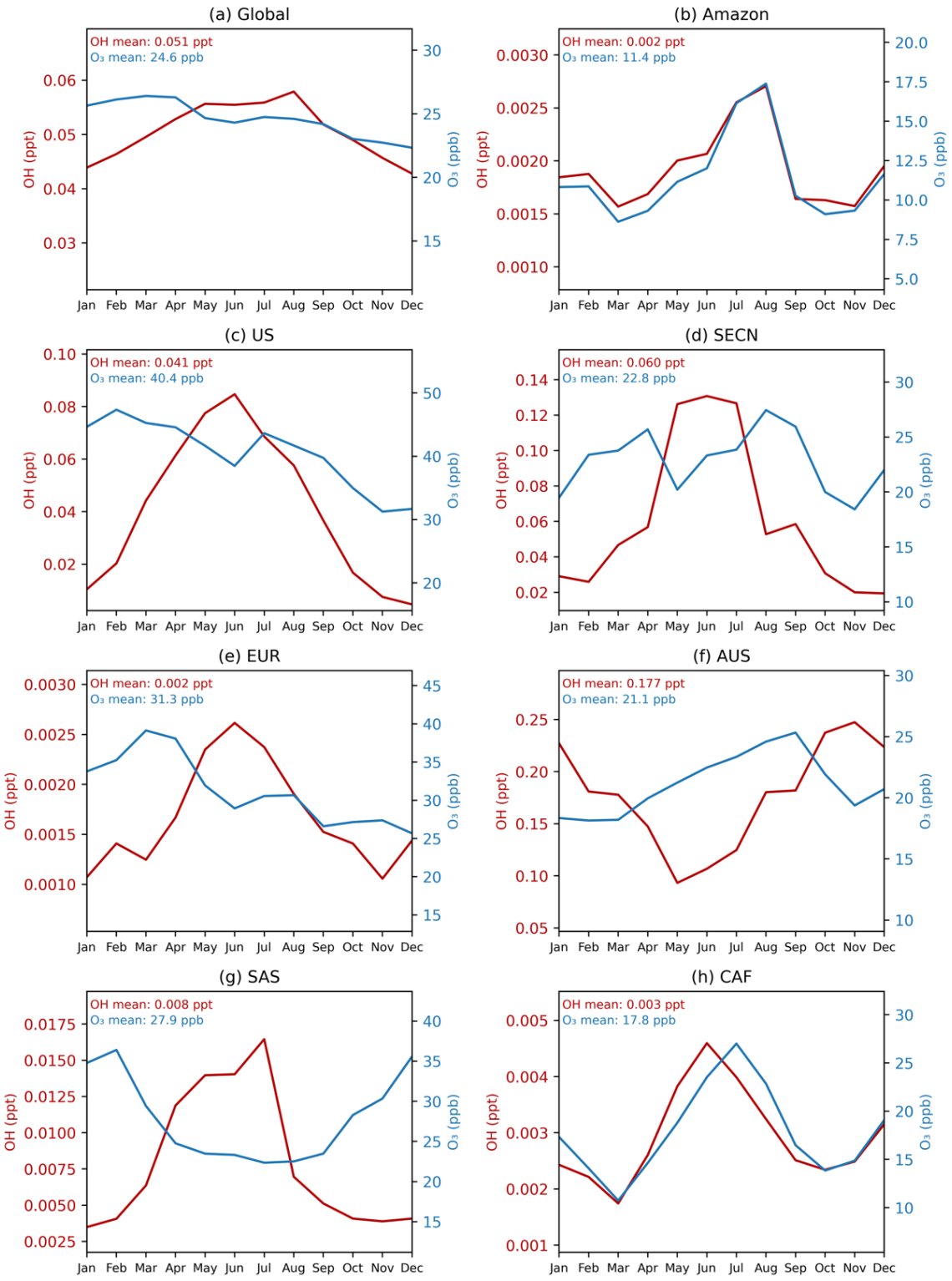

Figure 14. *Seasonal variations of OH and O_3 concentrations (ppt and ppb) in different regions. The mean OH and O_3 values for each region are shown in the upper right corner of each panel. Details of each geographic region can be found in Figure S9.*

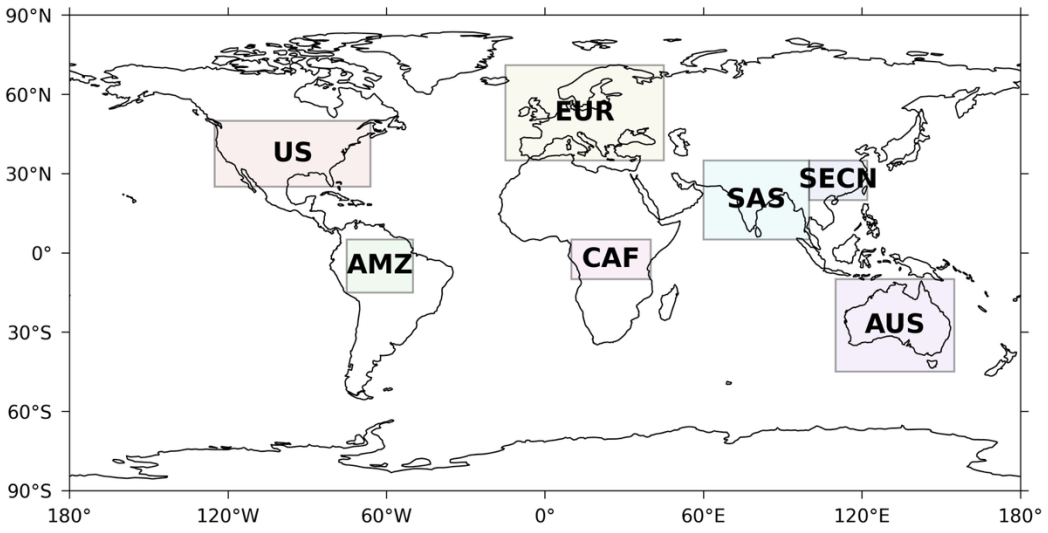

Figure S9. *Map showing the geographic locations of different regions analyzed in this study: Amazon Basin (AMZ), Continental U.S. (US), Southeastern China (SECN), Europe (EUR), Australia (AUS), South Asia (SAS), Central Africa (CAF).*

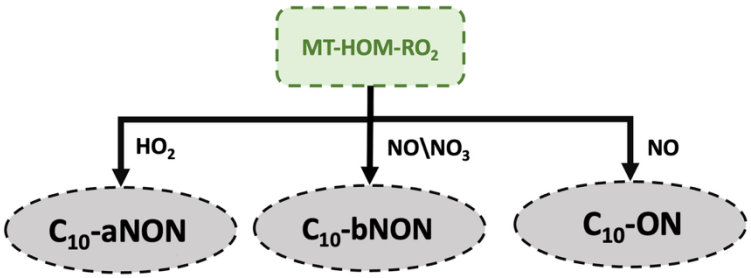

Figure 3*. Schematic diagram illustrating the oxidation of MT-HOM-RO₂ by HO₂, NO, or NO₃, leading to the formation of three types of gas-phase C₁₀ HOMs.*

We also add the following paragraph in Section 5 (Conclusion):

> *The seasonal variation of HOMs-SOA is largely influenced by the intensity of biogenic emissions, with oxidant levels playing a secondary regulatory role. The background levels of NO, oxidant concentrations, and wet deposition conditions in different regions collectively shape the HOMs-SOA formation process. In high NO emission regions (such as the United States, Southeast Asian Continental Regions, Europe, and South Asia), C₁₀-ON predominates, while in low NO emission regions with high biogenic emissions (such as the Amazon rainforest and central Africa), the proportion of dimers (C₁₅ and C₂₀) is significantly increased.*

2. Clarity of Reaction Mechanism Description

The description of the HOMs chemical mechanism in Section 2.2.2 and Figure 1 is currently quite dense and could be made clearer with a few structural adjustments. I recommend breaking the flowchart in Figure 1 into sub-panels, each representing a distinct stage of the mechanism, and aligning the discussion in the text with these steps using corresponding subsections or paragraphs. Additionally, it would be helpful to include a summary table outlining the key reaction pathways and their roles in forming C10, C15, and C20 HOMs. Finally, I suggest adopting clearer chemical nomenclatures and ensuring that all species and acronyms used in figures and tables are clearly defined in this section.

Response: Figure 1 was intended only as a conceptual overview of the key reaction pathways, not as a detailed representation of the entire chemical mechanism. We now recognize that this explanation could be further clarified. In response, we have divided the flowchart into sub-panels, each representing a distinct stage of the mechanism. After each sub-panel, a table summarizing the key chemical reactions has been added. Additionally, descriptions have been provided for each set of sub-panels and tables, offering an overview of the key reaction pathways and their roles in the formation of C_{10}, C_{15}, and C_{20}, while also clarifying the chemical nomenclature used throughout the section. The added sections are as follows:

2.2.2 Autoxidation

To account for the H-shift chemistry of MT-RO_2 leading to HOM formation (i.e., autoxidation), the first-generation monoterpene-derived RO_2 (MT-RO_2), formed via reactions of monoterpenes (MT) with OH or O_3, is classified into two categories: MT-aRO_2 and MT-bRO_2 (Fig. 1). Both categories undergo standard bimolecular reactions, but only MT-bRO_2 species proceed through autoxidation. In contrast, MT-aRO_2 species (such as APINO_2, BPINO_2, LIMONO_2, and MYRCO_2, listed in Table S12) do not participate in autoxidation.

Relatively high branching ratios for the formation of MT-bRO_2 are adopted, based on the values used in Table S3 of Xu et al. (2022). Specifically, the branching ratio of MT-bRO_2 is 0.75 for monoterpene + OH reactions, and 0.08 for monoterpene + O_3 reactions (Fig. 1). These values fall within the ranges reported in previous studies. Literature-based yields for MT-bRO_2 range from 0.075 to 0.83 for OH-initiated reactions (Lee et al., 2023; Piletic and Kleindienst, 2022; Pye et al., 2019; Weber et al., 2020; Xu et al., 2019) and from 0 to 0.22 for O_3-initiated reactions (Ehn et al., 2014; Jokinen et al., 2015; Roldin et al., 2019; Berndt et al., 2016; Kurtén et al., 2015; Richters et al., 2016). The reaction rate constants for OH and O_3 oxidation of monoterpenes are the same as those used in the default mechanism (Table 3), and apply equally to the formation of both MT-aRO_2 and MT-bRO_2. This approach is fully consistent with the implementation in GEOS-Chem by Xu et al. (2022), who demonstrated that such simplification can reasonably reproduce the formation of HOMs and the fate of RO_2 radicals. Furthermore, studies by Roldin et

al. (2019) and Weber et al. (2020) confirmed that using the same reaction rate for MT-bRO₂ and MT-aRO₂ also yields HOM concentrations that agree well with observations under forested conditions.

MT-bRO₂ are assumed to undergo one or multiple generations of autoxidation (Table 4). These reactions follow a temperature-dependent rate with an activation energy of 74.1 kJ/mol, consistent with previous studies (Lee et al., 2023; Möller et al., 2020; Pye et al., 2019; Roldin et al., 2019; Schervish and Donahue, 2020; Xu et al., 2019). The corresponding autoxidation rate are 0.27 s^{-1} at 283 K, 1.30 s^{-1} at 298 K, and 4.12 s^{-1} at 310 K. The yield of HOMs depends on both the autoxidation rate and the fraction of MT-RO₂ that undergoes autoxidation. To reflect the uncertainty associated with these parameters, this fraction is varied in both OH- and O₃-initiated pathways as part of sensitivity experiments. A detailed discussion of these tests is provided in Section 2.3.

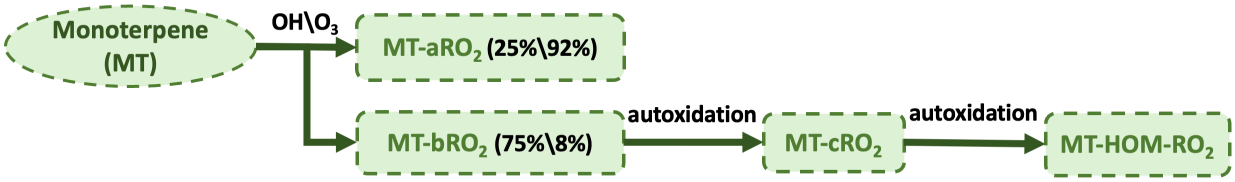

Figure 1. *Schematic of monoterpene (MT) oxidation and subsequent autoxidation pathways. MT reacts with OH or O₃ to form MT-aRO₂ or MT-bRO₂, with the latter undergoing autoxidation steps to yield HOMs. Branching ratios are shown for OH and O₃ pathways.*

Table 3. *Initial oxidation reactions of four representative monoterpenes (APIN, BPIN, LIMON, and MYRC) with OH and O₃, leading to the formation of MT-aRO₂ (non-autoxidizable) and MT-bRO₂ (autoxidizable). Detailed descriptions of the intermediate species are provided in Table S12.*

Index	*Reactions*	*Reaction rate*
1	*APIN[a] + OH → 0.25*MT-aRO₂ + 0.75*MT-bRO₂*	*1.34e-11*exp(410/T)*
2	*BPIN[a] + OH → 0.25*MT-aRO₂ + 0.75*MT-bRO₂*	*1.62e-11*exp(460/T)*
3	*LIMON[a] + OH → 0.25*MT-aRO₂ + 0.75*MT-bRO₂*	*3.41e-11*exp(470/T)*
4	*MYRC[a] + OH → 0.25*MT-aRO₂ + 0.75*MT-bRO₂*	*2.1e-10*
5	*APIN[a] + O₃ → 0.736*MT-aRO₂ + 0.064*MT-bRO₂ + 0.77*OH + 0.066*TERPA2O₂ + 0.22*H₂O₂ + 0.044*TERPA + 0.002*TERPACID + 0.034*TERPA2 + 0.17*HO₂ + 0.17*CO + 0.27*CH₂O + 0.054*TERPA2CO₃*	*1.34e-11*exp(410/T)*
6	*BPIN[a] + O₃ → 0.736*MT-aRO₂ + 0.064*MT-bRO₂ + 0.102*TERPK + 0.3*OH + 0.06*TERPA2CO₃ + 0.32*H₂O₂ +*	*1.62e-11* exp(460/T)*

	0.038*BIGALK + 0.19*CO_2 + 0.81*CH_2O + 0.11*HMHP + 0.08*HCOOH	
7	LIMON[a] + O_3 ⟶ 0.736*MT-aRO_2 + 0.064*MT-bRO_2 + 0.66*OH + 0.132*TERPF1 + 0.33*CH_3CO_3 + 0.33*CH_2O + 0.066*TERPA3CO_3 + 0.33*H_2O_2 + 0.002*TERPACID	3.41e-11*exp(470/T)
8	MYRC[a] + O_3 ⟶ 0.736*MT-aRO_2 + 0.064*MT-bRO_2 + 0.2*TERPF2 + 0.63*OH + 0.63*HO_2 + 0.25*CH_3COCH_3 +0.39*CH_2O + 0.18*HYAC	2.1e-10

[a] APIN, BPIN, LIMON, and MYRC represent α-pinene, β-pinene, limonene, and myrcene, respectively.

Table 4. *Autoxidation reactions of MT-bRO_2 leading to the formation of MT-cRO_2 and subsequently MT-HOM-RO_2.*

Index	Reactions	Reaction rate
9	MT-bRO_2 ⟶ MT-cRO_2	9.8e12*exp(-8836/T)
10	MT-cRO_2 ⟶ MT-HOM-RO_2	

2.2.3 Self-Reactions and Cross-Reactions

Due to isomers of MT-RO_2 and ISOP-RO_2, self- and cross-reactions are included (Table 5), with three branches considered for the products. First, intermediate products are produced and are lumped as C_{10}-ROH and C_{10}-CBYL. Second, RO radicals are generated, which may produce HO_2 and C_{10}-CBYL or decompose into smaller compounds. Half of the RO radicals are assumed to decompose into smaller carbonyls. Third, accretion products (C_{15} and C_{20}) are produced. The branching ratios of the three pathways above are set as 0.29:0.67:0.04, respectively (Xu et al., 2022). However, for the self- and cross-reactions involving MT-aRO_2 (A$PINO_2$, B$PINO_2$, L$IMONO_2$, and MYRCO_2 in Table S12) and ISOP-RO_2, a small fraction of RO radicals may undergo a unimolecular H-shift to form MT-bRO_2, with the branching ratio set to 0.05 (Xu et al., 2022). The fast reaction rate is applied here based on Table S4 in Xu et al. (2022).

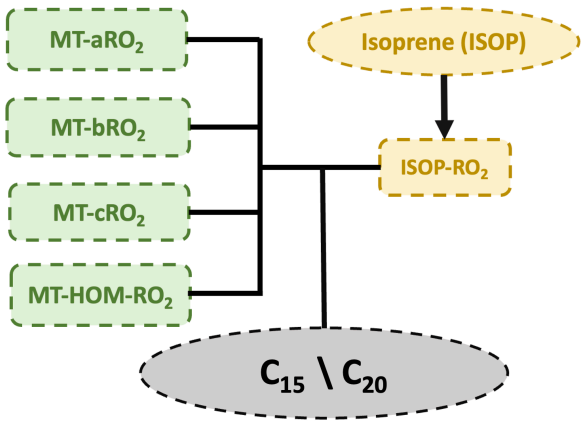

Figure 2. *Schematic illustration of self- and cross-reactions between MT-RO_2 and ISOP-RO_2 peroxy radicals.*

Table 5. *Summary of the self- and cross-reactions involving MT-RO_2 and ISOP-RO_2 peroxy radicals considered in this study. Detailed descriptions of the intermediate species are provided in Table S12.*

Index	*Reactions*	*Reaction rate*
11–20	*MT-aRO_2 + MT-aRO_2 → 0.893*C_{10}-CBYL + 0.29*C_{10}-ROH + 0.603*HO_2 + 1.34*HYDRALD + 0.067*MT-bRO_2 + 0.04* C_{20}*	*4.0e-11*
21–24	*MT-aRO_2 + MT-bRO_2 → 0.96*C10-CBYL + 0.29*C10-ROH + 0.67*HO2 + 1.34*HYDRALD + 0.04* C_{20}*	*4.0e-11*
25–28	*MT-aRO_2 + MT-cRO_2 → 0.96*C10-CBYL + 0.29*C10-ROH + 0.67*HO2 + 1.34*HYDRALD + 0.04* C_{20}*	*2.6e-10*
29–32	*MT-aRO_2 + MT-HOM-RO_2 → 0.96*C10-CBYL + 0.29*C10-ROH + 0.67*HO2 + 1.34*HYDRALD + 0.04* C_{20}*	*2.6e-10*
33–56	*MT-aRO_2 + ISOP-RO_2 → 0.4465*C10-CBYL + 0.145*C10-ROH + 0.145*ROH + 0.603*HO2+1.485*HYDRALD+0.0335*MT-bRO_2+ 0.04* C_{15}*	*2.0e-10*
57	*MT-bRO_2 + MT-bRO_2 → 0.96*C_{10}-CBYL + 0.29*C_{10}-ROH + 0.67*HO_2 + 1.34*HYDRALD + 0.04* C_{20}*	*4.0e-11*
58	*MT-cRO_2 + MT-cRO_2 → 0.96*C_{10}-CBYL + 0.29*C_{10}-ROH + 0.67*HO_2 + 1.34*HYDRALD + 0.04* C_{20}*	*2.6e-10*
59	*MT-HOM-RO_2 + MT-HOM-RO_2 → 0.96*C_{10}-CBYL + 0.29*C_{10}-ROH + 0.67*HO_2 + 1.34*HYDRALD + 0.04* C_{20}*	*2.6e-10*
60	*MT-bRO_2 + MT-cRO_2 → 0.96*C_{10}-CBYL + 0.29*C_{10}-ROH + 0.67*HO_2 + 1.34*HYDRALD + 0.04* C_{20}*	*2.6e-10*
61	*MT-bRO_2 + MT-HOM-RO_2 → 0.96*C_{10}-CBYL + 0.29*C_{10}-ROH + 0.67*HO_2 + 1.34*HYDRALD + 0.04* C_{20}*	*2.6e-10*
62	*MT-cRO_2 + MT-HOM-RO_2 → 0.96*C_{10}-CBYL + 0.29*C_{10}-ROH + 0.67*HO_2 + 1.34*HYDRALD + 0.04* C_{20}*	*2.6e-10*
63–68	*MT-bRO_2 + ISOP-RO_2 → 0.48*C_{10}-CBYL + 0.145*C_{10}-ROH + 0.145*ROH + 0.67*HO_2 + 1.485*HYDRALD + 0.04* C_{15}*	*2.0e-11*
69–74	*MT-cRO_2 + ISOP-RO_2 → 0.48*C_{10}-CBYL + 0.145*C_{10}-ROH + 0.145*ROH + 0.67*HO_2 + 1.485*HYDRALD + 0.04* C_{15}*	*4.0e-11*
75–80	*MT-HOM-RO_2 + ISOP-RO_2 → 0.48*C_{10}-CBYL + 0.145*C_{10}-ROH + 0.145*ROH + 0.67*HO_2 + 1.485*HYDRALD + 0.04* C_{15}*	*4.0e-11*

2.2.4 C_{10} HOMs formation

When MT-HOM-RO_2 are oxidized by HO_2, NO, or NO_3 (Fig. 3), three types of gas-phase C_{10} HOMs are formed: two types of C_{10} non-nitrate HOMs (C_{10}-aNON and C_{10}-bNON) and C_{10} nitrate HOMs (C_{10}-ON), as shown in Table 6. The rate constants used are the same as those for the MT-RO_2 + HO_2, NO, and NO_3 reactions in Xu et al. (2022).

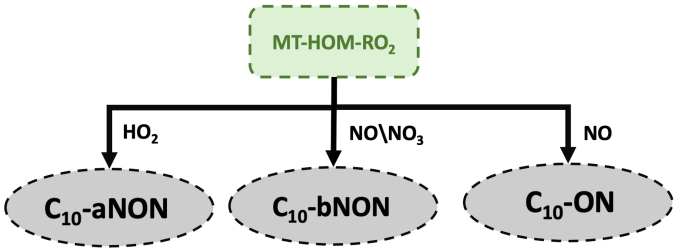

***Figure 3**. Schematic diagram illustrating the oxidation of MT-HOM-RO_2 by HO_2, NO, or NO_3, leading to the formation of three types of gas-phase C_{10}-HOMs.*

***Table 6.** C_{10} HOMs formation. Detailed descriptions of the intermediate species are provided in Table S12.*

Index	*Reactions*	*Reaction rate*
109	*MT-HOM-RO_2 + HO_2 → C_{10}-aNON + O_2*	*1.5e-11*
110	*MT-HOM-RO_2 + NO → 0.8*NO_2 + 0.8*HO_2 + 0.4* C_{10}-bNON + 0.8*HYDRALD + 0.2* C_{10}-ON*	*4.0e-12*
111	*MT-HOM-RO_2 + NO_3 → HO_2 + NO_2 + 0.5* C_{10}-bNON + HYDRALD*	*1.2e-12*

3. Justification for Excluding NO_3-Initiated HOMs

The manuscript excludes NO3-initiated HOMs due to uncertainties. While this is understandable, recent studies suggest this pathway may be more important than previously thought. Therefore, a brief discussion of their potential importance (especially in polluted nighttime conditions) would provide a perspective for this HOM formation pathway.

Response: Sorry for ignoring the role of NO_3-initiated oxidation pathways in our previous discussion. We have revised the manuscript in Lines 138 to 150 (the underlined content is newly added or modified):

> *The MT-RO_2 formed by the oxidation of monoterpenes by NO_3 radicals is not considered in this study, as some studies report that the branching ratio remains highly uncertain ~~to be insignificant~~ (Zhao et al., 2021; Nah et al., 2016; Yan et al., 2016; Roldin et al., 2019)~~, and the chemical process remains highly uncertain (Roldin et al., 2019)~~.*

Additionally, the following discussion has been added in Section 5 (Conclusion):

This study investigates the formation of HOMs from monoterpene oxidation in a global simulation, yet significant uncertainties remain in the representation of NO_3-initiated pathways. Recent studies suggest that NO_3-initiated HOM formation may be more important than previously thought, particularly under polluted nighttime conditions. Chamber experiments on α- and β-phellandrene oxidation by NO_3 have shown significant SOA and HOM production, with SOA yields reaching approximately 35% and 60%, respectively, accompanied by abundant HOM monomers and dimers (Harb et al., 2024). Furthermore, field observations from the southeastern United States indicate that NO_3 remains the dominant oxidant of monoterpenes at night, accounting for around 60% (observed) to 80% (modeled) of total monoterpene oxidation (Desai et al., 2024). These results highlight the potential importance of NO_3-initiated HOM formation in contributing to organic aerosol formation under polluted nighttime conditions. However, due to structural differences in monoterpenes, such as ring strain and double-bond position, HOM yields vary widely among different species (Dam et al., 2022; Draper et al., 2024) and are highly sensitive to ambient NO_x concentrations and humidity (Pasik et al., 2025; Li et al., 2022). The incomplete understanding of these mechanisms limits the accuracy of HOM predictions in models. Future research should combine field observations, laboratory constraints, and updated reaction schemes to reduce these uncertainties and improve global-scale modeling of nighttime organic aerosol formation.

Minor Comments

• Lines 45–46: The introduction discusses the role of HOMs in radiative forcing, but this is not revisited in the results. Including even a qualitative discussion in the results or conclusions on how HOMs-SOA might influence regional or global climate would enhance the impact of the study.

Response: Thank you for your suggestion. We have added the following content to the conclusion section (Section 5) to address how HOMs-SOA might influence climate:

> *On a global scale, the formation of HOMs-SOA is influenced not only by chemical reaction mechanisms but also by their potential to indirectly affect radiative forcing through changes in cloud condensation nuclei (CCN). In particular, in tropical regions such as the Amazon and central Africa, where HOMs-SOA concentrations are high, the generated CCN could significantly influence the marine low cloud areas on the western side of continents. These changes in CCN may alter cloud droplet size and cloud reflectivity, thereby impacting the regional radiative balance.*

• Lines 89–90: Please provide references for the models mentioned.
• Lines 90–95: Include details on the simulation period used in the study.

Response: We have added the reference in lines 89–90 and included details on the simulation period used in the study. The revised text is as follows (the underlined content is newly added or modified):

> *The Community Atmosphere Model version 6 with comprehensive tropospheric and stratospheric chemistry (CAM6-Chem) from the Community Earth System Model version 2.1.0 (CESM2.1.0) is used in this study (Danabasoglu et al., 2020). The default configuration of CAM6-Chem employs the four-mode version of the Modal Aerosol Module (MAM4) (Liu et al., 2016) and applies the Volatility Basis Set (VBS) approach (Donahue et al., 2006; Hodzic et al., 2016; Jo et al., 2021; Robinson et al., 2007) to represent the formation of SOA from all volatile organic compounds (VOCs). All simulations are configured with a horizontal resolution of 0.95° in latitude and 1.25° in longitude and a vertical resolution of 32 layers up to approximately 40 km (Emmons et al., 2020). Meteorological fields, including temperature, winds, and surface fluxes, from the Modern-Era Retrospective analysis for Research and Applications (MERRA2) reanalysis data set (Gelaro et al., 2017) are used for offline nudging to minimize uncertainties in meteorology simulation (Jo et al., 2021; Tilmes et al., 2019; Liu et al., 2021). Anthropogenic and biomass burning emissions are from the standard Coupled Model Intercomparison Project 6 (CMIP6) (Eyring et al., 2016). The biogenic emissions are simulated online using the Model of Emissions of Gases and Aerosol from Nature version2.1 (MEGAN2.1) (Guenther et al., 2012).*

The simulation period spanned from June to July 2013 and from April to June 2014, corresponding to the field campaign periods (SENEX and BAECC, see Section 2.3), and was used to evaluate model improvements (with one month for spin-up). Additionally, to assess the contribution of different chemical reaction pathways in the formation of HOMs and the spatiotemporal distribution of HOMs-SOA, we conducted one-year simulations for 2013 (with one month for spin-up) across different sensitivity experiments (see Section 2.4).

• Lines 99–100: Specify the total amounts of monoterpene and isoprene emissions considered in the simulations.

Response: Thank you for your comment. The spatial distribution of monoterpene and isoprene emissions is shown in Figure S4. The temporal distribution (global and for key regions) is presented in Figure 13.

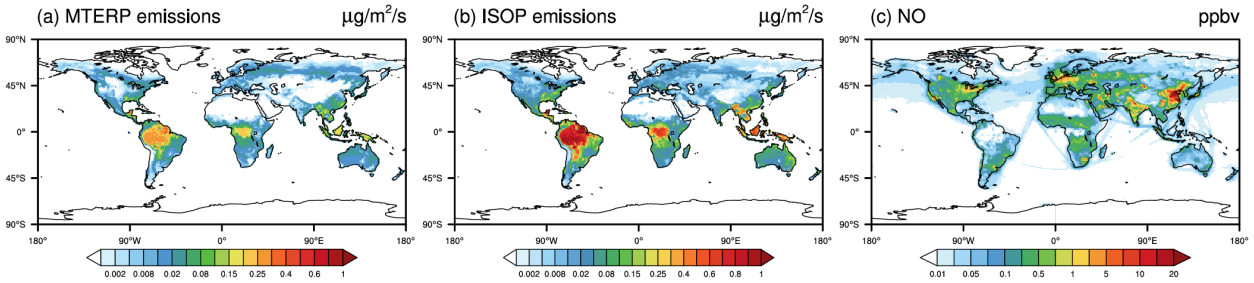

Figure S4. 2013 annual averaged surface (a) MTERP emissions (unit: μg/m³/s), (b) ISOP emissions (unit: μg/m³/s), (c) NO concentration (unit: ppbv) in Control experiment.

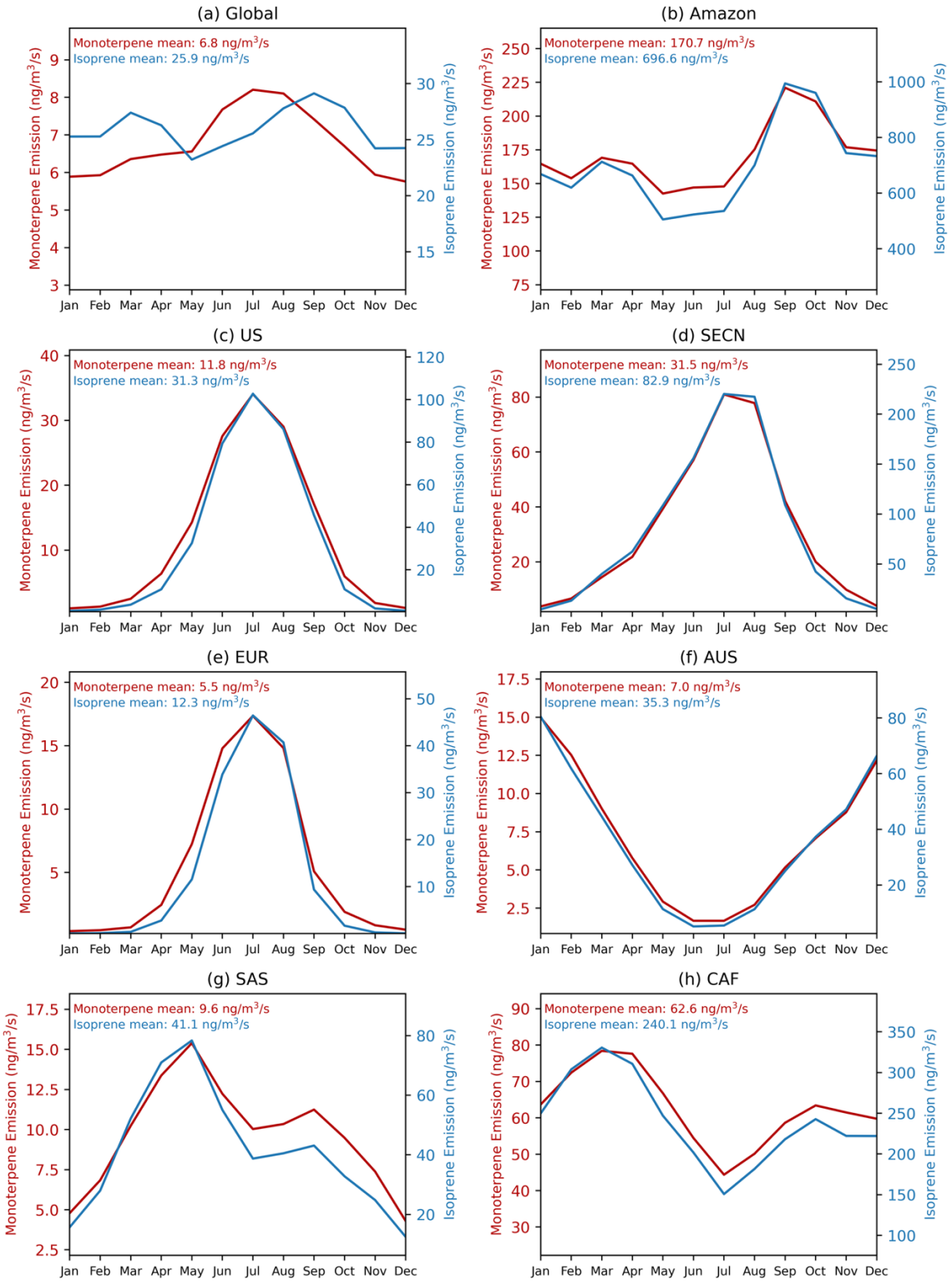

Figure 13. *Seasonal variations in monoterpene and isoprene emissions (ng/m³/s) across different regions. The average annual emissions for each species are provided in the caption. Details of each geographic region can be found in Figure S9.*

• Lines 114–115: Please rephrase this sentence, the current wording is difficult to follow.

Response: Thank you for your feedback. We have rephrased the sentence to improve clarity and readability. The revised sentence is as follows:

SOA ~~are formed when emitted volatile organic compounds (VOCs) are oxidized in the atmosphere with subsequent gas-particle partitioning processes or new particle formation.~~ are generated when volatile organic compounds (VOCs) undergo oxidation, leading to the formation of low-volatility gases that subsequently condense onto pre-existing aerosols.

• Line 125: In addition to the vapor pressure equation, please include the gas-particle partitioning equation used in the model.

Response: We thank the reviewer for this helpful suggestion. We have added a description of the gas–particle partitioning approach based on the absorptive equilibrium theory (Pankow, 1994). In the revised manuscript, we have added the following content to the main text:

The SOAG in different volatility bin (SOAG0~4 in Table 1) condenses on the preexisting aerosols to form SOA (soa1~5 in Table 1) based on their saturation vapor pressure calculated following Eqn. (1) (Chung and Seinfeld, 2002):

$$P_{0,i}(T) = P_{0,i}(T_0) \cdot e^{\left[\frac{-\Delta H_{vap}}{R}\left(\frac{1}{T}-\frac{1}{T_0}\right)\right]} \quad (1)$$

where $P_{0,i}(T)$ is the saturation vapor pressure at temperature T and T_0=298 K; R is the ideal gas constant, and ΔH_{vap} is the enthalpies of vaporization which represents the energy to transform the liquid substance into gas phase (default parameterized values shown in ***Error! Reference source not found.****).*

For SOA species i and aerosol mode m, the equilibrium gas concentration is expressed as:

$$g_i^* = \frac{g_{0,i}}{M_{OA}} \times A_i \quad (2)$$

$g_{0,i}$ is the equilibrium gas mixing ratio derived from the saturation vapor pressure (Eqn. (1) and specifically shown in Eqn. (3)), A_i is the particle-phase concentration of species i, and M_{OA} is the total absorbing organic mass (including SOA and oxidized POA).

$$g_{0,i} = \frac{P_{0,i}(T)}{P} \quad (3)$$

where P is the atmospheric pressure.

The dynamic exchange between gas and particle phases is described by a first-order mass transfer equation:

$$\frac{dA_i}{dt} = (G_i - g_i^*) \times k_i \quad (4)$$

where G_i is the gas-phase concentration and k_i is the transfer coefficient. This formulation ensures mass conservation and is solved using a semi-implicit numerical scheme. Similar approaches are widely used in global climate models to represent SOA gas–particle partitioning within the volatility basis set (VBS) framework (Pankow, 1994; Donahue et al., 2006; Tilmes et al., 2015).

• Line 189: The field campaigns referenced here have not yet been introduced. Consider moving this sentence or providing context earlier.

Response: we have swapped the order of Sections 2.3 (Sensitivity experiments) and 2.4 (Observations) to provide context for the field campaigns earlier in the manuscript. This adjustment ensures that the field campaigns are introduced before they are referenced in Line 189. The detailed description of the observations (Section 2.3) will be provided in the next response.

• Section 2.4: This section should be expanded. Please include more details about the field campaigns, the types of measurements conducted, the instruments used, and a brief summary of key findings relevant to the model evaluation.

Response: We thank the reviewer for the helpful suggestion. In response, we have expanded Section 2.4 (which is now Section 2.3) to include more detailed information about the field campaigns. The updated Section 2.3 is as follows:

Data from two campaigns were used for comparison: the Southern Oxidant and Aerosol Study (SOAS) in the southeastern USA, and the Biogenic Aerosols – Effects on Clouds and Climate (BAECC) in Hyytiälä, Finland (Carlton et al., 2018; Martin et al., 2016; Petäjä et al., 2016) (Table 8). HOM measurements were obtained using high-resolution time-of-flight chemical ionization mass spectrometer (HRToF-CIMS) when available (Lopez-Hilfiker et al., 2014). For HOM measurements, molecular formulas of compounds containing 10 carbon atoms and at least 7 oxygen atoms were selected as HOMs. The compounds with one nitrate and without nitrate were compared to the simulated C_{10}-aNON, C_{10}-bNON, and C_{10}-ON, respectively. In addition to HOMs, related species such as NO, O_3, monoterpenes, and isoprene were also compared when the data was available (Figs. S1 and S2). The primary HOM species identified in the SENEX (Southeast Nexus) and BAECC campaigns (Tables S15 and S16).

Table 7. *Field campaigns used in this paper*

Campaigns	*Dates*	*Locations*
SOAS (Warneke et al., 2016)	*2013.06.01–07.15*	*Centreville, Alabama, US (32.93°N, 87.13°W)*
BAECC (Petäjä et al., 2016)	*2014.04.11–06.03*	*Station for Measuring Ecosystem Atmosphere Relations (SMEAR II), Hyytiälä, Finland. (61.85°N，24.28°E）*

Table S15. *Molecular formulas of top 5 contributing HOM-ON and HOM-NON species (gas- and particle-phase) at Centreville, Alabama*

HOM-ON		***HOM-NON***	
Gas-phase	***Particle-phase***	***Gas-phase***	***Particle-phase***
C10H15O7N1	*C10H15O7N1*	*C10H14O7*	*C10H14O7*
C10H17O7N1	*C10H15O8N1*	*C10H12O7*	*C10H12O7*
C10H15O8N1	*C10H17O7N1*	*C10H22O8*	*C10H16O7*
C10H17O8N1	*C10H17O8N1*	*C10H22O7*	*C10H22O8*
C10H13O8N1	*C10H15O9N1*	*C10H16O7*	*C10H22O7*

Table S16. *Molecular formulas of top 5 contributing HOM-ON and HOM-NON species (gas- and particle-phase) at Hyytiälä, Finland*

HOM-ON		***HOM-NON***	
Gas-phase	***Particle-phase***	***Gas-phase***	***Particle-phase***
C10H15O7N1	*C10H15O8N1*	*C10H12O11*	*C10H14O7*
C10H15O8N1	*C10H15O7N1*	*C10H14O8*	*C10H22O9*
C10H17O7N1	*C10H17O7N1*	*C10H16O8*	*C10H22O7*
C10H13O7N1	*C10H17O8N1*	*C10H14O7*	*C10H22O8*
C10H17O8N1	*C10H15O9N1*	*C10H22O7*	*C10H16O7*

• Lines 225–226: This sentence appears more appropriate for the conclusions section rather than the results.

Response: The original sentence in lines 225–226 is as follows:

> *Addressing these gaps requires coordinated laboratory measurements and targeted ambient observations to disentangle competing chemical processes.*

We have removed this sentence in the results and, recognizing the relevance of this issue for observational efforts, we have included a directional description in the final paragraph of the conclusion:

> *To address persistent gaps between model predictions and observations, field campaigns targeting accretion product speciation and chamber studies that constrain MT-bRO$_2$ branching ratios are needed.*

• Section 3.3: Consider moving the global model results to a new standalone Section 4 to give them greater emphasis and allow for a more structured discussion.

Response: We have added an additional section (Section 4) to describe the spatiotemporal variation of HOMs-SOA. For further details, please refer to the response to the first major comment.

• Figures 7b–7c: Consider applying a minimum threshold for MTSOA (7b) and SOA (7c) before calculating the contributions of HOMs. Reporting high percentage contributions in regions with negligible SOA concentrations may be misleading and could skew global averages.
• Figures 8b, 8d, 8f, 8h: The same recommendation applies as for Figures 7b and 7c.

Response: Thank you for your suggestion. In response, we have revised the original Figures 7 and 8 and replaced them with the following two updated figures.

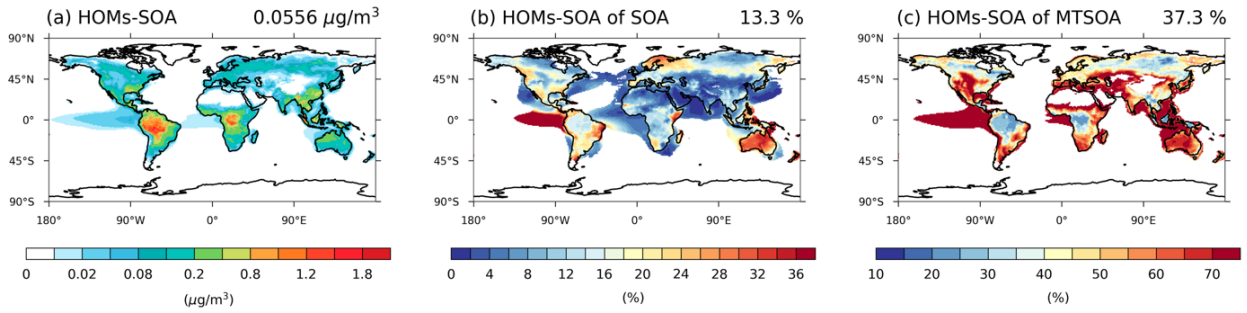

Figure 10. *2013 annual averaged surface (a) HOMs-SOA (unit: μg/m^3), (b) the contribution of HOMs-SOA to the MTSOA and (c) the contribution of HOMs-SOA to the total SOA (unit: %) in Control experiment. The global averaged value is shown in upper right corner of each figure. Proportions are only shown in regions where MTSOA or total SOA is greater than 10% of the global average.*

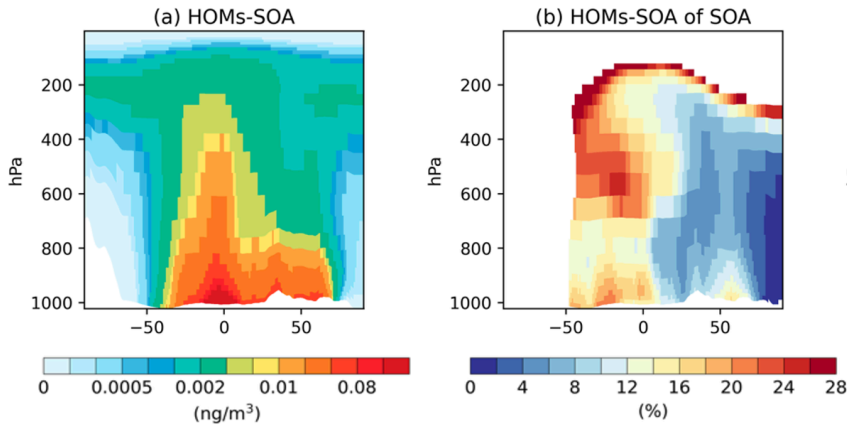

Figure 11. *Vertical distribution of 2013 annual averaged (a) HOMs-SOA concentration (μg/m^3) and (b) proportion of HOMs-SOA to total SOA (%) in the Control experiment. The global average value is shown in the upper right corner of each panel. Proportions are only shown in regions where total SOA is greater than 10% of the global average.*

• Terminology: Ensure consistent use of terms such as "C10-NON", "C10-ON", and "HOMs-SOA" throughout the manuscript and figures.

Response: We have carefully reviewed the manuscript and ensured consistent use of terms such as "C_{10}-NON", "C_{10}-ON", and "HOMs-SOA" throughout the text and figures.

• Supplement: The supplementary material is well-organized and informative. It would be helpful to reference specific tables and figures more explicitly in the main text to guide the reader.

Response: We have made some adjustments to the supplementary material, removing tables and figures that were not cited in the main text.

Reference

Berndt, T., Richters, S., Jokinen, T., Hyttinen, N., Kurten, T., Otkjaer, R. V., Kjaergaard, H. G., Stratmann, F., Herrmann, H., Sipila, M., Kulmala, M., and Ehn, M.: Hydroxyl radical-induced formation of highly oxidized organic compounds, Nat Commun, 7, 13677, 10.1038/ncomms13677, 2016.

Chung, S. H. and Seinfeld, J. H.: Global distribution and climate forcing of carbonaceous aerosols, Journal of Geophysical Research: Atmospheres, 107, AAC 14-11-AAC 14-33, https://doi.org/10.1029/2001JD001397, 2002.

Dam, M., Draper, D. C., Marsavin, A., Fry, J. L., and Smith, J. N.: Observations of gas-phase products from the nitrate-radical-initiated oxidation of four monoterpenes, Atmos. Chem. Phys., 22, 9017–9031, https://doi.org/10.5194/acp-22-9017-2022, 2022.

Desai, N. S., Moore, A. C., Mouat, A. P., Liang, Y., Xu, T., Takeuchi, M., Pye, H. O. T., Murphy, B., Bash, J., Pollack, I. B., Peischl, J., Ng, N. L., and Kaiser, J.: Impact of Heatwaves and Declining NOx on Nocturnal Monoterpene Oxidation in the Urban Southeastern United States, Journal of Geophysical Research: Atmospheres, 129, e2024JD041482, https://doi.org/10.1029/2024JD041482, 2024.

Donahue, N. M., Robinson, A. L., Stanier, C. O., and Pandis, S. N.: Coupled partitioning, dilution, and chemical aging of semivolatile organics, Environmental Science & Technology, 40, 2635-2643, 10.1021/es052297c, 2006.

Draper, D., Almeida, T. G., Iyer, S., Smith, J. N., Kurtén, T., and Myllys, N.: Unpacking the diversity of monoterpene oxidation pathways via nitrooxy–alkyl radical ring-opening reactions and nitrooxy–alkoxyl radical bond scissions, J. Aerosol Sci., 179, 106379, https://doi.org/10.1016/j.jaerosci.2024.106379, 2024.
Ehn, M., Thornton, J. A., Kleist, E., Sipila, M., Junninen, H., Pullinen, I., Springer, M., Rubach, F., Tillmann, R., Lee, B., Lopez-Hilfiker, F., Andres, S., Acir, I. H., Rissanen, M., Jokinen, T., Schobesberger, S., Kangasluoma, J., Kontkanen, J., Nieminen, T., Kurten, T., Nielsen, L. B., Jorgensen, S., Kjaergaard, H. G., Canagaratna, M., Maso, M. D., Berndt, T., Petaja, T., Wahner, A., Kerminen, V. M., Kulmala, M., Worsnop, D. R., Wildt, J., and Mentel, T. F.: A large source of low-volatility secondary organic aerosol, Nature, 506, 476-479, 10.1038/nature13032, 2014.

Jokinen, T., Berndt, T., Makkonen, R., Kerminen, V. M., Junninen, H., Paasonen, P., Stratmann, F., Herrmann, H., Guenther, A. B., Worsnop, D. R., Kulmala, M., Ehn, M., and Sipila, M.: Production of extremely low volatile organic compounds from biogenic emissions: Measured yields and atmospheric implications, Proc Natl Acad Sci U S A, 112, 7123-7128, 10.1073/pnas.1423977112, 2015.
Kurten, T., Rissanen, M. P., Mackeprang, K., Thornton, J. A., Hyttinen, N., Jorgensen, S., Ehn, M., and Kjaergaard, H. G.: Computational Study of Hydrogen Shifts and Ring-Opening Mechanisms in alpha-Pinene Ozonolysis Products, J Phys Chem A, 119, 11366-11375, 10.1021/acs.jpca.5b08948, 2015.

Harb, S., Cirtog, M., Alage, S., Cantrell, C., Cazaunau, M., Michoud, V., Pangui, E., Bergé, A., Giorio, C., Battaglia, F., and Picquet-Varrault, B.: HOMs and SOA formation from the oxidation of α- and β-phellandrenes by NO3 radicals, EGUsphere [preprint], https://doi.org/10.5194/egusphere-2024-3419, 2024.

Lee, B. H., Iyer, S., Kurtén, T., Varelas, J. G., Luo, J., Thomson, R. J., and Thornton, J. A.: Ring-opening yields and auto-oxidation rates of the resulting peroxy radicals from OH-oxidation of α-pinene and β-pinene, Environmental Science: Atmospheres, 3, 399-407, 10.1039/d2ea00133k, 2023.

Li, D.; Huang, W.; Wang, D.; Wang, M.; Thornton, J. A.; Caudillo, L.; Rorup, B.; Marten, R.; Scholz, W.; Finkenzeller, H.; Marie, G.; Baltensperger, U.; Bell, D. M.; Brasseur, Z.; Curtius, J.; Dada, L.; Duplissy, J.; Gong, X.; Hansel, A.; He, X. C.; Hofbauer, V.; Junninen, H.; Krechmer, J. E.; Kurten, A.; Lamkaddam, H.; Lehtipalo, K.; Lopez, B.; Ma, Y.; Mahfouz, N. G. A.; Manninen, H. E.; Mentler, B.; Perrier, S.; Petaja, T.; Pfeifer, J.; Philippov, M.; Schervish, M.; Schobesberger, S.; Shen, J.; Surdu, M.; Tomaz, S.; Volkamer, R.; Wang, X.; Weber, S. K.; Welti, A.; Worsnop, D. R.; Wu, Y.; Yan, C.; Zauner-Wieczorek, M.; Kulmala, M.; Kirkby, J.; Donahue, N. M.; George, C.; El-Haddad, I.; Bianchi, F.; Riva, M. Nitrate Radicals Suppress Biogenic New Particle Formation from Monoterpene Oxidation. Environ. Sci. Technol. 2024, 58 (3), 1601−1614.

Nah, T., Sanchez, J., Boyd, C. M., and Ng, N. L.: Photochemical Aging of α-pinene and β-pinene Secondary Organic Aerosol formed from Nitrate Radical Oxidation, Environ. Sci. Technol., 50, 222-231, 10.1021/acs.est.5b04594, 2016.

Pankow, J.: An absorption model of the gas/aerosol partitioning involved in the formation of secondary organic aerosol, Atmos. Environ., 28, 189, 1994.

Pasik, D., Golin Almeida, T., Ahongshangbam, E., Iyer, S., and Myllys, N.: Monoterpene oxidation pathways initiated by acyl peroxy radical addition, Atmos. Chem. Phys., 25, 4313–4331, https://doi.org/10.5194/acp-25-4313-2025, 2025.

Petäjä, T., O'Connor, E. J., Moisseev, D., Sinclair, V. A., Manninen, A. J., Väänänen, R., von Lerber, A., Thornton, J. A., Nicoll, K., Petersen, W., Chandrasekar, V., Smith, J. N., Winkler, P. M., Krüger, O., Hakola, H., Timonen, H., Brus, D., Laurila, T., Asmi, E., Riekkola, M.-L., Mona, L., Massoli, P., Engelmann, R., Komppula, M., Wang, J., Kuang, C., Bäck, J., Virtanen, A., Levula, J., Ritsche, M., and Hickmon, N.: BAECC: A Field Campaign to Elucidate the Impact of Biogenic Aerosols on Clouds and Climate, Bull. Amer. Meteor. Soc., 97, 1909-1928, https://doi.org/10.1175/BAMS-D-14-00199.1, 2016.

Pye, H. O. T., D'Ambro, E. L., Lee, B. H., Schobesberger, S., Takeuchi, M., Zhao, Y., Lopez-Hilfiker, F., Liu, J., Shilling, J. E., Xing, J., Mathur, R., Middlebrook, A. M., Liao, J., Welti, A., Graus, M., Warneke, C., de Gouw, J. A., Holloway, J. S., Ryerson, T. B., Pollack, I. B., and Thornton, J. A.: Anthropogenic enhancements to production of highly oxygenated molecules from autoxidation, Proc Natl Acad Sci U S A, 116, 6641-6646, 10.1073/pnas.1810774116, 2019.

Roldin, P., Ehn, M., Kurten, T., Olenius, T., Rissanen, M. P., Sarnela, N., Elm, J., Rantala, P., Hao, L., Hyttinen, N., Heikkinen, L., Worsnop, D. R., Pichelstorfer, L., Xavier, C., Clusius, P., Ostrom, E., Petaja, T., Kulmala, M., Vehkamaki, H., Virtanen, A., Riipinen, I., and Boy, M.: The role of highly oxygenated organic molecules in the Boreal aerosol-cloud-climate system, Nat Commun, 10, 4370, 10.1038/s41467-019-12338-8, 2019.

Schervish, M. and Donahue, N. M.: Peroxy radical chemistry and the volatility basis set, Atmos. Chem. Phys., 20, 1183–1199, https://doi.org/10.5194/acp-20-1183-2020, 2020.

Shao, X., Wang, M., Dong, X., Liu, Y., Shen, W., Arnold, S. R., Regayre, L. A., Andreae, M. O., Pöhlker, M. L., Jo, D. S., Yue, M., and Carslaw, K. S.: Global modeling of aerosol nucleation with a semi-explicit chemical mechanism for highly oxygenated organic molecules (HOMs), Atmos. Chem. Phys., 24, 11365–11389, https://doi.org/10.5194/acp-24-11365-2024, 2024.

Shao, X., Wang, M., Dong, X., Liu, Y., Arnold, S. R., Regayre, L. A., Jo, D. S., Shen, W., Wang, H., Yue, M., Wang, J., Zhang, W., and Carslaw, K. S.: The effect of organic nucleation on the indirect radiative forcing with a semi-explicit chemical mechanism for highly oxygenated organic molecules (HOMs), EGUsphere [preprint], https://doi.org/10.5194/egusphere-2024-4135, 2025.

Stolzenburg, D., Fischer, L., Vogel, A. L., Heinritzi, M., Schervish, M., Simon, M., Wagner, A. C., Dada, L., Ahonen, L. R., Amorim, A., Baccarini, A., Bauer, P. S., Baumgartner, B., Bergen, A., Bianchi, F., Breitenlechner, M., Brilke, S., Buenrostro Mazon, S., Chen, D., Dias, A., Draper, D. C., Duplissy, J., El Haddad, I., Finkenzeller, H., Frege, C., Fuchs, C., Garmash, O., Gordon, H., He, X., Helm, J., Hofbauer, V., Hoyle, C. R., Kim, C., Kirkby, J., Kontkanen, J., Kürten, A., Lampilahti, J., Lawler, M., Lehtipalo, K., Leiminger, M., Mai, H., Mathot, S., Mentler, B., Molteni, U., Nie, W., Nieminen, T., Nowak, J. B., Ojdanic, A., Onnela, A., Passananti, M., Petäjä, T., Quéléver, L. L. J., Rissanen, M. P., Sarnela, N., Schallhart, S., Tauber, C., Tomé, A., Wagner, R., Wang, M., Weitz, L., Wimmer, D., Xiao, M., Yan, C., Ye, P., Zha, Q., Baltensperger, U., Curtius, J., Dommen, J., Flagan, R. C., Kulmala, M., Smith, J. N., Worsnop, D. R., Hansel, A., Donahue, N. M., and Winkler, P. M.: Rapid growth of organic aerosol nanoparticles over a wide tropospheric temperature range, P. Natl. Acad. Sci. USA, 115, 9122–9127, https://doi.org/10.1073/pnas.1807604115, 2018.

Tilmes, S., Lamarque, J. F., Emmons, L. K., Kinnison, D. E., Ma, P. L., Liu, X., Ghan, S., Bardeen, C., Arnold, S., Deeter, M., Vitt, F., Ryerson, T., Elkins, J. W., Moore, F., Spackman, J. R., and Val Martin, M.: Description and evaluation of tropospheric chemistry and aerosols in the Community Earth System Model (CESM1.2), Geoscientific Model Development, 8, 1395-1426, 10.5194/gmd-8-1395-2015, 2015.

Warneke, C., Trainer, M., de Gouw, J. A., Parrish, D. D., Fahey, D. W., Ravishankara, A. R., Middlebrook, A. M., Brock, C. A., Roberts, J. M., Brown, S. S., Neuman, J. A., Lerner, B. M., Lack, D., Law, D., Hubler, G., Pollack, I., Sjostedt, S., Ryerson, T. B., Gilman, J. B., Liao, J., Holloway, J., Peischl, J., Nowak, J. B., Aikin, K., Min, K. E., Washenfelder, R. A., Graus, M. G., Richardson, M., Markovic, M. Z., Wagner, N. L., Welti, A., Veres, P. R., Edwards, P., Schwarz, J. P., Gordon, T., Dube, W. P., McKeen, S., Brioude, J., Ahmadov, R., Bougiatioti, A., Lin, J. J., Nenes, A., Wolfe, G. M., Hanisco, T. F., Lee, B. H., Lopez-Hilfiker, F. D., Thornton, J. A., Keutsch, F. N., Kaiser, J., Mao, J., and Hatch, C.: Instrumentation and Measurement Strategy for the NOAA SENEX Aircraft Campaign as Part of the Southeast Atmosphere Study 2013, Atmos Meas Tech, 9, 3063-3093, 10.5194/amt-9-3063-2016, 2016.

Weber, J., Archer-Nicholls, S., Griffiths, P., Berndt, T., Jenkin, M., Gordon, H., Knote, C., and Archibald, A. T.: CRI-HOM: A novel chemical mechanism for simulating highly oxygenated organic molecules

(HOMs) in global chemistry–aerosol–climate models, Atmos. Chem. Phys., 20, 10889-10910, 10.5194/acp-20-10889-2020, 2020.

Xu, L., Moller, K. H., Crounse, J. D., Otkjaer, R. V., Kjaergaard, H. G., and Wennberg, P. O.: Unimolecular Reactions of Peroxy Radicals Formed in the Oxidation of alpha-Pinene and beta-Pinene by Hydroxyl Radicals, J Phys Chem A, 123, 1661-1674, 10.1021/acs.jpca.8b11726, 2019.

Yan, C., Nie, W., Äijälä, M., Rissanen, M. P., Canagaratna, M. R., Massoli, P., Junninen, H., Jokinen, T., Sarnela, N., Häme, S. A. K., Schobesberger, S., Canonaco, F., Yao, L., Prévôt, A. S. H., Petäjä, T., Kulmala, M., Sipilä, M., Worsnop, D. R., and Ehn, M.: Source characterization of highly oxidized multifunctional compounds in a boreal forest environment using positive matrix factorization, Atmos. Chem. Phys., 16, 12715-12731, 10.5194/acp-16-12715-2016, 2016.

Xu, R. C., Thornton, J. A., Lee, B., Zhang, Y. X., Jaegle, L., Lopez-Hilfiker, F. D., Rantala, P., and Petaja, T.: Global simulations of monoterpene-derived peroxy radical fates and the distributions of highly oxygenated organic molecules (HOMs) and accretion products, Atmos. Chem. Phys., 22, 5477-5494, 10.5194/acp-22-5477-2022, 2022.

Zhao, B., Fast, J. D., Donahue, N. M., Shrivastava, M., Schervish, M., Shilling, J. E., Gordon, H., Wang, J., Gao, Y., Zaveri, R. A., Liu, Y., and Gaudet, B.: Impact of Urban Pollution on Organic-Mediated New-Particle Formation and Particle Number Concentration in the Amazon Rainforest, Environ Sci Technol, 55, 4357-4367, 10.1021/acs.est.0c07465, 2021.

Zhao, B., Donahue, N. M., Zhang, K., Mao, L., Shrivastava, M., Ma, P.-L., Shen, J., Wang, S., Sun, J., Gordon, H., Tang, S., Fast, J., Wang, M., Gao, Y., Yan, C., Singh, B., Li, Z., Huang, L., Lou, S., Lin, G., Wang, H., Jiang, J., Ding, A., Nie, W., Qi, X., Chi, X., and Wang, L.: Global variability in atmospheric new particle formation mechanisms, Nature, 631, 98-105, 10.1038/s41586-024-07547-1, 2024.